To appear in *Advanced Robotics*
Vol. 00, No. 00, XX 20XX, 1–24

Full paper

Development and Field Test of the Articulated Mobile Robot T^2 Snake-4 for Plant Disaster Prevention

Motoyasu Tanaka[a]*, Kazuyuki Kon[b], Mizuki Nakajima[a], Nobutaka Matsumoto[a], Shinnosuke Fukumura[a], Kosuke Fukui[a], Hidemasa Sawabe[a], Masahiro Fujita[c], and Kenjiro Tadakuma[c]

[a]*Department of Mechanical Intelligent Systems Engineering, Graduate School of Information Science and Engineering, The University of Electro-Communication, 1-5-1 Chofugaoka, Chofu, Tokyo, Japan*;
[b]*National Security Solutions Division, NEC Corporation, 1-10 Nisshin-cho, Tokyo, Japan*;
[c]*Department of Applied Information Sciences, Graduate School of Information Sciences, Tohoku University, 6-6-01 Aramaki Aza Aoba, Aoba-ku, Sendai, Miyagi, Japan*;

(*v1.0 released XX 20XX*)

In this work, we develop an articulated mobile robot that can move in narrow spaces, climb stairs, gather information, and operate valves for plant disaster prevention. The robot can adopt a tall position using a folding arm and gather information using sensors mounted on the arm. In addition, this paper presents a stair climbing method using single backward wave. This method enables the robot to climb stairs that have a short tread. The developed robot system is tested in a field test at the World Robot Summit 2018, and the lessons learned in the field test are discussed.

Keywords: articulated mobile robot; snake robot; plant inspection; stairs;

1. Introduction

Equipment malfunctions can lead to serious accidents involving human injuries in big industrial plants that handle hazardous materials, for example, oil and gas plants. Equipment inspection is routinely carried out in such plants to avoid serious accidents. If there is an equipment malfunction, it is inappropriate for a human to directly gather information on site because of the danger of explosion. Therefore, plant inspection robots for inspecting equipment and addressing malfunctions have been developed [1, 2], and some competitions on this topic have been held [3–5].

The ARGOS (Autonomous Robot for Gas and Oil Sites) challenge [3, 4] was held to develop a robot for both daily equipment inspection and information gathering in abnormal situations. In the competition, two challenges were held: one was an autonomous mission for the scenario of daily inspection, and the other was a remote-control mission for the scenario of an abnormal situation. In this challenge, to demonstrate mobility, it was necessary for the robot to avoid/climb obstacles and to climb stairs. To demonstrate the ability to take measurements, the robot needed to autonomously detect the value of pressure gauges, valve positions, and temperature of an object. The participating teams used crawler robots (AIR-K [7] and VIKINGS [10]), crawler robots with a multi-jointed arm on which sensors were mounted (ARGONAUTS [8] and FOXIRIS), and a four-legged robot (LIO [9]).

The robot competition World Robot Summit 2018 (WRS2018) [5] took placed in Tokyo, Japan, in October 2018. Nine challenges in four categories were carried out in the competition.

*Corresponding author. Email: mtanaka@uec.ac.jp

Table 1. Properties of T^2 Snake-3 and T^2 Snake-4 for plant inspection.

Property	T^2 Snake-3 with the gripper [17]	T^2 Snake-4
Accessibility	The robot cannot access locations high above the ground by itself. It can climb a 1-m step, but it then moves by leaning toward the vertical plane of the step.	A folding arm is mounted to access locations high above the ground (Section 2.3).
Graspability	The robot cannot grasp large valves in a plant because of the small radius of its gripper.	A larger gripper is mounted for grasping large valves (Section 2.3).
Measurement ability	The only sensors for inspection are two visible light cameras on the head and tail.	In addition to visible light cameras, other types of sensors are mounted (Section 2.4).
Mobility	If stairs in a plant have a short tread, the robot cannot climb them using the method of [16].	A method for climbing stairs with short tread is implemented (Section 3.2).

In the disaster robotics category, one challenge was the Plant Disaster Prevention Challenge [6]. The themes of the challenge were daily inspections, tests, and the emergency responses taken when faults occur at industrial plants. In the challenge, it was necessary for competitors to carry out missions that simulated daily inspection, equipment calibration, equipment diagnosis, initial fire-fighting, and disaster response. The robot prepared by the participating team needs to move while passing through narrow spaces and climbing stairs in a field that simulates an industrial plant. The robot needs not only to gather information but also to rotate valves located in the field. The valve rotation task is of the differences of this challenge with respect to the ARGOS challenge. To complete the missions, it is necessary for the robot to have high mobility, measurement ability, and manipulation ability for valve rotation. Thus, it can be said that WRS2018 is a good scenario in which to carry out a field test for plant inspection robots.

The articulated mobile robot [11] has links serially connected by joints, and each link has a mechanism that generates propulsion force. The robot can pass through narrow spaces, climb obstacles, and climb stairs [12–16] because it has a long thin body and high mobility. In addition, the robot can work using an end-effector similar to [17–19] because the entire body of the robot is similar to the manipulator. These features are suitable for plant inspection. We have developed the articulated mobile robot T^2 Snake-3 [16, 17], which passes through narrow spaces, climbs a 1-m step, semi autonomously climbs stairs, and rotates valves using a soft gripper. However, assuming that the task of the robot is to inspect a plant, these abilities are not enough.

In the present study, we developed the T^2 Snake-4 articulated mobile robot for plant inspection, and demonstrated the usefulness of the developed robot system in a field test at WRS2018. The contributions of this paper are as follows.

- T^2 Snake-4, which is an articulated mobile robot for plant inspection, is developed. Its ability to access locations high above the ground, grasping ability for valve rotation, and measurement ability are better than those of the previous robot T^2 Snake-3[16].
- A stair climbing method using a single backward traveling wave is proposed. Using the proposed method, the robot can climb stairs with shallow treads that it could not climb using the previous method [16].
- We participated in the WRS2018 Plant Disaster Prevention Challenge as a field test, and the proposed system was tested.

2. System of T^2 Snake-4

Figure 1 shows the articulated mobile robot T^2 Snake-4. The robot was developed for plant inspection, and is based on the T^2 Snake-3 [16, 17]. T^2 Snake-4 was developed to solve the problems of T^2 Snake-3, as listed in Table 1.

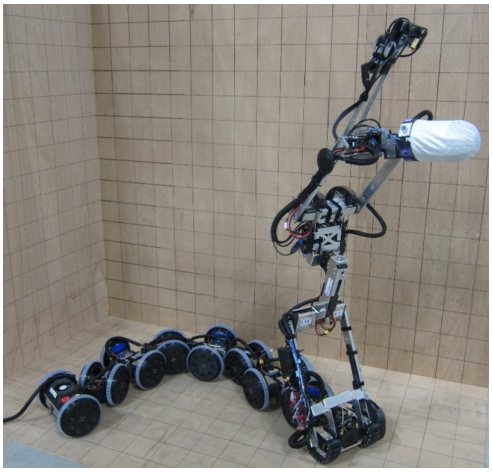

Figure 1. Articulated mobile robot T^2 Snake-4 (wired version).

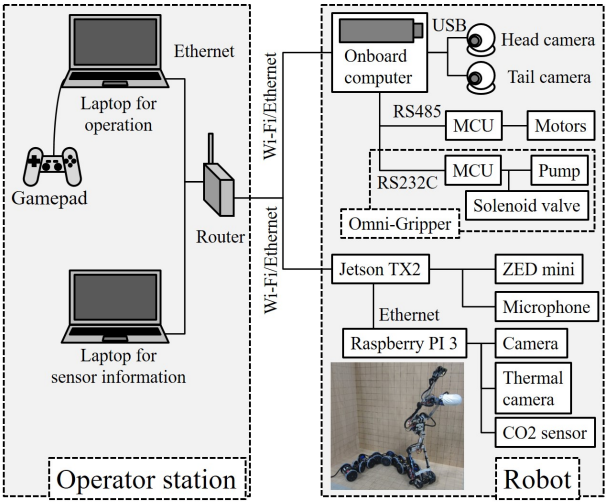

Figure 2. Overall system of the developed robot

2.1 *Overall system and operator station*

Figure 2 shows the overall system of the developed robot. There are two laptops in the operator station; one is for operating the robot, and the other is for visualizing the sensor information. The gamepad, which sends commands to the robot, is connected to the laptop for operation. The two laptops are connected to a router by an ethernet cable. The robot operating system (ROS) is used as the robot's middleware, and the laptops and robot communicate on the intranet through the router.

2.2 *Base part*

T^2 Snake-4 is composed of a base and a folding arm. The base has active joints and active wheels. Figure 3 shows a model of the base. We define a *module* to be a group of two links and a yaw joint between the two links. The modules are serially connected by the pitch joint, and a pair of active wheels are coaxially placed with respect to the pitch joint. Figure 4 shows the details of the base. We use the Dynamixel XM540-W270R and XM430-W350-R (Robotis Co., Ltd.) as actuators for the joint and wheel, respectively. The composition of joints and wheels is almost the same as those of the ACM-R4 series [20–22] and T^2 Snake-3 [16, 17]. On the head, there

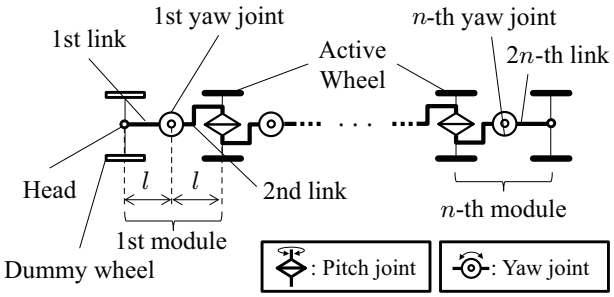

Figure 3. Model of the base of the robot.

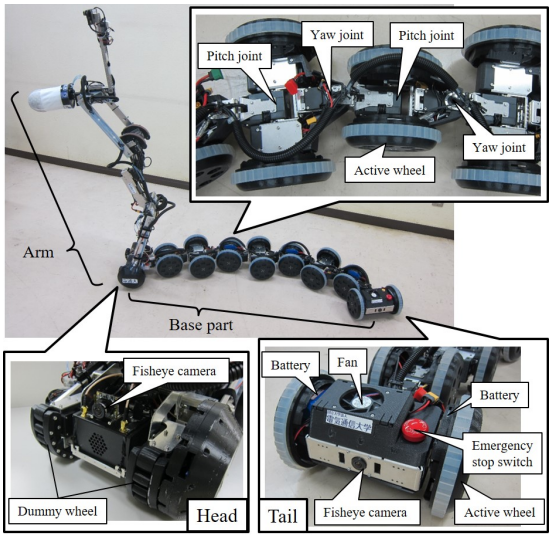

Figure 4. Detail of the base of the robot.

are two dummy wheels that have many passive rollers, a fisheye camera, and the Jetson TX2, which functions as processor for the sensor information. On the tail, the onboard computer (an Intel compute stick) for controlling the robot and another fisheye camera are mounted. Many microcomputer units (MCUs), which are mounted on various positions on the body, intermediate between the actuators and the onboard computer, in common with T^2 Snake-3. Table 2 compares the specifications of the T^2 Snake-4 and T^2 Snake-3 of [16, 17].

In the base, the main improvements with respect to the T^2 Snake-3 are as follows.

- All wheels are independently rotated by motors to improve mobility.
- A grouser structure is introduced on the outer surface of the wheel to improve mobility.
- Storage spaces are generated while maintaining the rotational range of the yaw joint by alternately connecting the wide link and narrow link as in [17].
- The wheel radius is enlarged to improve the moving speed of the robot and generate the storage spaces.

Note that the robot width is larger than T^2 Snake-3. The width of narrow spaces in the competition field was described as approximate 600 mm in the rulebook of the competition, and the robot width has been smaller than it.

The lithium polymer batteries HP-G550-1300S4 and HP-G760C1800S4 are stored in the internal spaces of the wheels and the storage space at the side of the pitch joint. The batteries, which supply power to the actuators, are connected with a relay circuit, and the power supply is controlled by an emergency stop switch on the tail.

Table 2. Specifications of T^2 Snake-4, T^2 Snake-3 with a gripper [17], and T^2 Snake-3 [16].

	T^2 Snake-4	T^2 Snake-3 with a gripper [17]	T^2 Snake-3 [16]
Number of modules	8	9	9
Number of arm joints	8	2	0
Link length l [mm]	90.5	90.5	90.5
Module length L [mm]	181	181	181
Height* [mm]	218	175	120
Width [mm]	Arm: 320 Base: 250	175	150
Length** [mm]	1,598	1,729	1,729
Wheel radius r [mm]	75	50	50
Total mass [kg]	20	10	9.2
Battery life [min]	about 60	about 80	about 80

* Height when the robot is in a posture that minimises its height.

** Length without the arm when the robot adopts a straight posture.

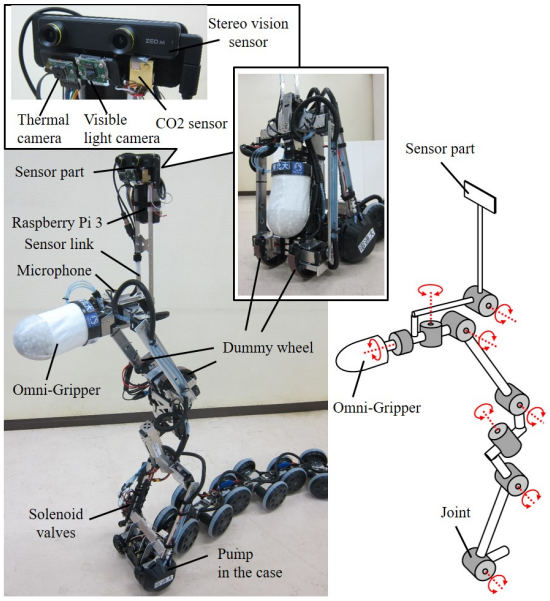

Figure 5. Folding arm and its joint configuration.

2.3 *Folding arm*

Figure 5 shows the details of the folding arm. The arm has eight joints, and the joint that needs to exert a large torque is actuated in parallel by two actuators. Seven joints are used to move the gripper and the remaining joint is used to independently move the sensor part, on which many types of sensors are attached. There are two dummy wheels in the arm, and the robot uses them to touch the surrounding terrain when climbing a step and stairs.

The improved version of the Omni-Gripper is attached to the tip of the arm as the end-effector. This is a soft gripper that is more resistant to cutting than the previous gripper of [23]. In addition, the size of the gripper is increased so that it can grasp a larger valve. Its weight is 554 g and its diameter is 100 mm. Two lithium polymer batteries are stored on the arm to supply power to the arm and gripper. Additional details of the folding arm will be reported in another paper [24].

2.4 *Sensors*

Many types of sensors are attached on the robot for executing missions. The fisheye cameras on the head and tail are used to obtain views of the surroundings when the operator controls the

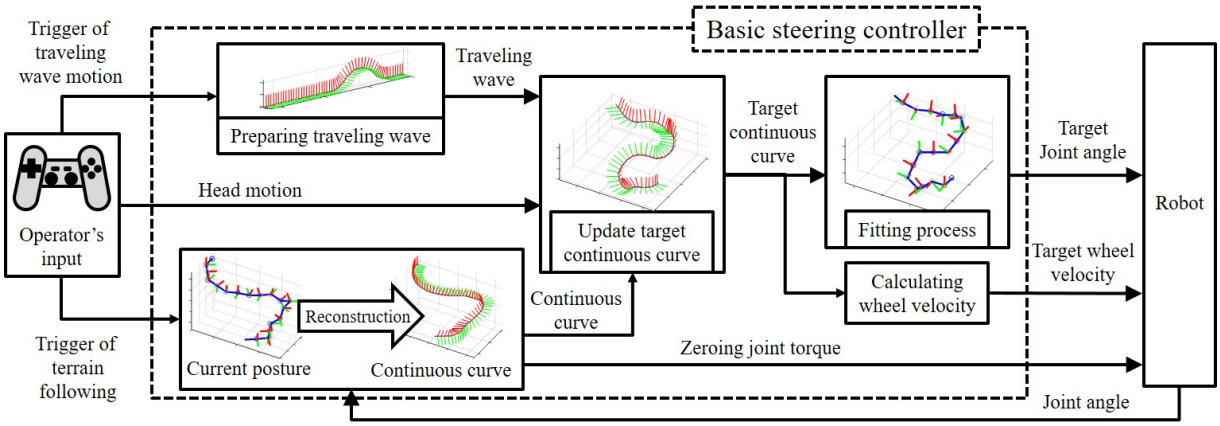

Figure 6. Basic steering controller.

robot. The onboard computer obtains not only the views of the fisheye cameras but also angle, current, and error information of all the actuators. The obtained data is sent to the operator station using the ROS network.

On the sensor part, as shown in Fig. 5, there are a visible light cameras (Pi camera module v2) to obtain the view of the operation by the gripper, a thermal camera (Lepton 3.0), and a CO2 sensor (MH-Z19) to detect abnormalities, and a stereo vision sensor (ZED mini) for visual simultaneous localization and mapping (Visual SLAM). The microphone is attached near the tip of the arm to detect abnormal noise. The data from the stereo vision sensor and microphone are processed at the Jetson TX2. A Raspberry Pi 3 Model B+ obtains the data of the visible light camera, thermal camera, and CO2 sensor, and sends them to the Jetson TX2 through an ethernet cable. The Jetson TX2 sends all obtained data to the operator station using the ROS network.

3. Control for locomotion

This section describes basic steering and stair climbing methods for the proposed robot. The control method for an end-effector using the folding arm will be presented in [24].

3.1 *Basic steering method*

The basic steering controller proposed in [16] is implemented in the robot. Figure 6 shows a block diagram of the controller. The controller employs a three-dimensional steering method based on the shape-fitting method of [21, 25]. In addition, the terrain-following and traveling wave motions of [16] are included. For details of the equation, the reader is referred to [16].

In the shape-fitting method, the target posture is represented as a continuous curve and the target angles of the joints are approximately calculated by fitting the robot to a curve. In addition, the rotational velocities of the wheels are also calculated based on a continuous curve. The continuous curve is updated considering the motion of the head of the robot generated by the operator's commands. This control method is also called *shift control* because the motion shifts from the head to the tail.

A traveling wave motion is used to recover the robot from a stuck state. In this motion, the target continuous curve is overlapped with a traveling wave. The region of the body that has become stuck in the surrounding terrain is lifted by the traveling wave so that the robot can recover from the stuck state. The traveling wave and terrain-following motions are executed when triggered by the operator.

The robot uses the terrain-following motion [16] to follow the complicated terrain. When

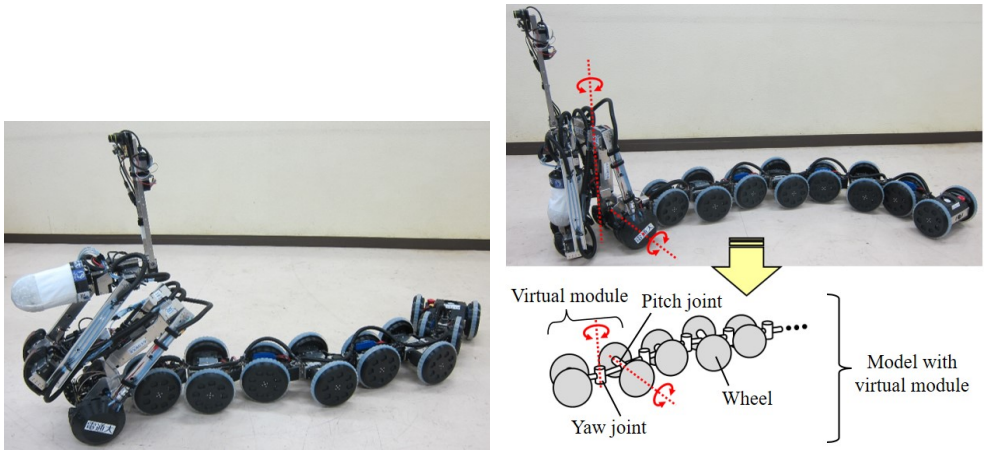

(a) Using only the base.

(b) Using the virtual module.

(c) Elongating the virtual module.

Figure 7. The robot in basic steering control.

the robot uses terrain following, it follows the surrounding terrain by zeroing the torque of the joints. The robot can move forward while following the terrain by resuming the three-dimensional steering method from the zeroed joint torque posture. Here, the target continuous curve is reconstructed from the current posture of the robot.

Two handling methods for the folding arm are provided in the basic steering method. One is a method in which the arm is folded, as shown in Fig. 7(a), and the basic steering method is used for only the base. The operator sends the command to the robot while observing the views of the fisheye cameras on the head and tail. This method is not suitable for climbing obstacles because the entire arm is lifted and a large joint torque is needed. The other method is basic steering control while considering the folding arm. The arm can be treated as one unit of the body (a yaw joint, pitch joint, and pair of wheels). We call the unit corresponding to the arm the *virtual module*. If the robot uses this method, the joint torque when the robot climbs obstacles is smaller than in the case shown in Fig. 7(a) (basic steering control without the virtual module) because the dummy wheels in the arm also touch the ground. In addition, the robot can climb a higher obstacle by elongating the virtual module, as shown in Fig. 7(c). Note that the yaw joint in the virtual module cannot be used when elongating the virtual module.

3.2 *Stair climbing method using a single backward traveling wave*

In [26], a flexible mono-tread mobile track was developed. This robot can climb stairs and spiral stairs when the friction condition is satisfied because the entire bottom of the body of the robot generates a propulsion force. In contrast, articulated mobile robots have joint parts that do not generate propulsion force. If the joint part contacts the edge of the stairs, the robot may become stuck. Articulated mobile robots where the crawler units are serially connected by elastic joints

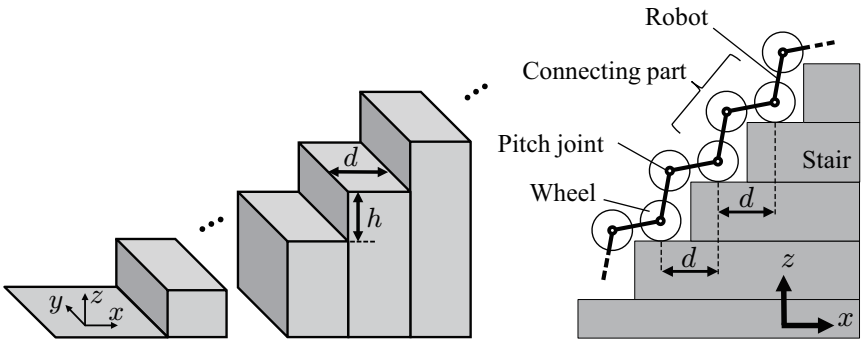

(a) Stairs

(b) Basic posture of the robot when climbing stairs

Figure 8. Stairs and basic posture of the robot.

have successfully climbed stairs, e.g. [12]. The ACM-R8 [14] can determine the terrain using torque sensors and can climb stairs using its large wheel. These robots can climb stairs because they have large propulsion mechanisms and the joint parts do not often contact the stairs.

The other approach for climbing stairs without becoming stuck is to appropriately adjust the joint motion. OT-4[13] has climbed stairs using a reinforcement learning system called the *7G control system*. An inchworm robot [27] can climbed stairs, but the sequential method was only applied to a five-link robot and very wide range of joint angle is needed to execute the method. Snake robots without wheels have succeeded in climbing stairs using the pre-scripted gait of [28] and a crawler gait of [29].

In [16], the semiautonomous stair climbing method of T^2 Snake-3 was proposed. The robot appropriately rotates the joints so that the joint part does not contact the stair, and the grounded/ungrounded information of the wheels detected by the range sensor is used to trigger the joint motion. The robot places the wheels one by one on the next step using the joint motion of the method, and can climb up steep stairs without falls caused by slippage. However, this method cannot be used if the length of the links of the robot are large or the tread of the stairs is short.

This subsection presents a stair climbing method so that the robot can climbs stairs that it cannot climb using [16]. The motion of a backward traveling wave is used by earthworms [30] and large snakes like boas [31], and they locomote by generating the wave by elongating and contracting their body. This motion has been used in earthworm robots [32, 33]. These robots can move forward by shifting the elongating link from the head to tail. The basic steering control presented in Section 3.1 can be thought of as a kind of backward traveling waves because the head motion shifts from the head to tail.

In [15], an articulated mobile robot that has crawler units connected by only the pitch joint has climbed stairs, using a simple backward traveling wave whose wavelength is adjusted to fit the character of the terrain. However, no specific description using mathematical formulas was reported. The robot does not have a yaw joint and the distance between adjacent units is very small. This means that the joint part is unlikely to contact the surrounding terrain and it is hard for the robot to become stuck. In contrast, the region of the joint part in the entire body of the robot developed in the paper is larger than that of [15] because the developed robot has both a pitch joint and yaw joint at the joint part. This means that it is easy for the joint part of the robot to contact the surroundings. If the robot uses a backward traveling wave without considering the relative relationship between itself and the stairs, it is possible for the robot to become stuck or fall down. Thus, we designed a novel stair climbing motion for the articulated mobile robot so that it can avoid becoming stuck or falling.

Figure 8(a) shows the stairs assumed in this section. The riser heights and tread depths are

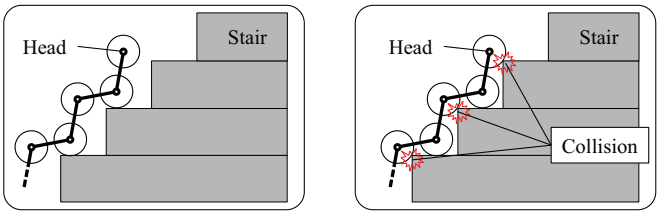

(a) Before moving forward (b) After moving forward

Figure 9. Stair climbing motion for step 1.

all the same. We define that depth d satisfies the condition

$$r \leq d < L + r, \tag{1}$$

where L is the module length of the robot and r is the wheel radius, as shown in Fig. 3 and Table 2. The robot cannot climb stairs whose parameters satisfy condition (1) using the method of [16]. The arm is treated as a virtual module similar to the case of basic steering control considering the folding arm. We assume that the robot approaches the stairs parallel to the x axis, as shown in Fig. 8(a).

The posture shown in Fig. 8(b) is used as the basic posture of the robot when climbing stairs. One pair of wheels contacts one tread. The part of the body connecting two treads is called the connecting part. The posture of the connecting part is designed so that the distance between the contact points between the robot and tread is d along the x axis. We assume that the connecting part consists of two modules and the angle of the yaw joint on the connecting part is zero, as in [16]. Then, d, h, and L have to satisfy the following condition.

$$d^2 + h^2 \leq 4L^2. \tag{2}$$

In the proposed method, the robot climbs the stairs step by step by shifting the *elongating part* from the head to tail like a backward traveling wave. Concretely, the robot repeats the following three steps.

Step 1: The entire body of the robot moves forward to adjust the relative position between the robot and stairs, as shown in Fig. 9.
Step 2: The head section becomes the elongated part, as shown in Fig. 10.
Step 3: The elongated part is shifted backward, as shown in Fig. 11. The robot returns to step 1 if the elongated part disappears.

The appropriate position in step 1 is designed to depend on the contact point of the wheel when the elongated part is generated. If the forward movement is not sufficient, the wheel at the tip of the elongated part cannot touch the next step when generating the next elongated part. If we appropriately design the angles of the connecting part, we can determine whether the relative position is appropriate by determining whether the lifted wheel of the connecting part touches the edge of the next step, as shown in Fig. 9.

In step 2, there are three cases, as Fig. 10 shows, depending on the situation of the head. Cases 1 and 2 occur when the next step exists, and case 3 is for the case where the next step does not exist.

In step 3, if the wheels on the tread move backward, it is possible that the wheels have separated from the tread. This triggers a likely fall for the robot. Thus, we designed the shift so that the positions of the ith and $(i+4)$th wheel in Figs. 11(a) and (b) are maintained where ith wheel is the most anterior wheel in the elongating part. As a result, the position of the wheels that are not related to the shift are maintained. Let θ_i be the absolute angle of the ith module,

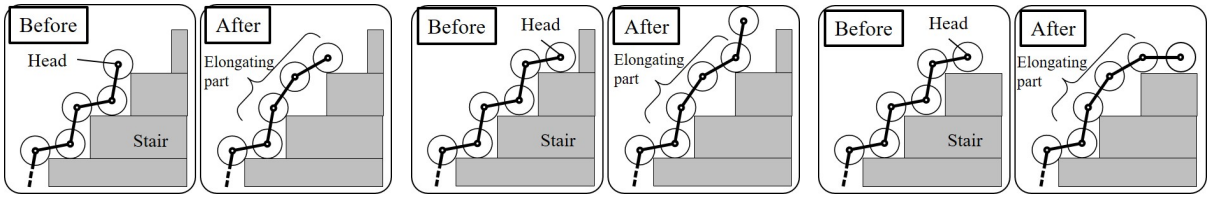

(a) Case 1 (b) Case 2 (c) Case 3

Figure 10. Stair climbing motion for step 2.

and α_1, α_2, β_1, and β_2 be the absolute angles of the connecting part and elongated part, as Fig. 12 illustrates. These angles are calculated as

$$\alpha_1 = 2\mathrm{atan2}\left(\frac{2Lh - \sqrt{(d^2+h^2)(4L^2-d^2-h^2)}}{d^2+2Ld+h^2}\right), \tag{3}$$

$$\alpha_2 = 2\mathrm{atan2}\left(\frac{2Lh + \sqrt{(d^2+h^2)(4L^2-d^2-h^2)}}{d^2+2Ld+h^2}\right), \tag{4}$$

$$\beta_1 = 2\mathrm{atan2}\left(\frac{2Ll_\mathrm{z} - \sqrt{(l_\mathrm{x}^2+l_\mathrm{z}^2)(4L^2-l_\mathrm{x}^2-l_\mathrm{z}^2)}}{l_\mathrm{x}^2+2Ll_\mathrm{x}+l_\mathrm{z}^2}\right), \tag{5}$$

$$\beta_2 = 2\mathrm{atan2}\left(\frac{2Ll_\mathrm{z} + \sqrt{(l_\mathrm{x}^2+l_\mathrm{z}^2)(4L^2-l_\mathrm{x}^2-l_\mathrm{z}^2)}}{l_\mathrm{x}^2+2Ll_\mathrm{x}+l_\mathrm{z}^2}\right), \tag{6}$$

where

$$l_\mathrm{x} = d + \Delta\bar{x} + \Delta l, \tag{7}$$

$$l_\mathrm{z} = 2h - L\sin\alpha_2, \tag{8}$$

$\Delta\bar{x}$ is the position between the third wheel of the elongating part and the contact point along x axis, and $\Delta l \geq 0$ is a design parameter to change the x position of the first wheel in the elongating part as Fig. 12. The contact point between the robot and the stair is categorized as four cases according to the parameters as Fig. 13. Let l_b be the distance between the center and the bottom of the link. $\Delta\bar{x}$ can be geometrically calculated considering Fig. 13. (3) and (4) have a solution without imaginary parts because of (2). If (5) and (6) have a solution without imaginary parts, the following condition has to be satisfied.

$$l_\mathrm{x}^2 + l_\mathrm{z}^2 \leq 4L^2 \tag{9}$$

Figure 14 shows the relationship between d and the maximum h which is numerically obtained in the case where $\Delta l = 0.01$ m, $L = 0.181$ m, $r = 0.075$ m, and $l_\mathrm{b} = 0.025$ m. Let the start time of the shift be $t = 0$ and the end time of the shift be $t = t_\mathrm{shift}$. If the shift from Figs. 11(a) to (b) is carried out, we design the joint angles according to the following geometric relationships as Fig. 15.

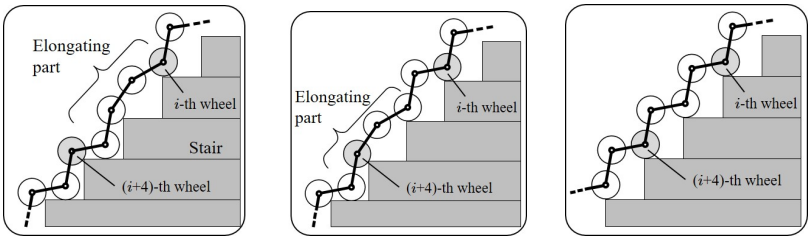

(a) Before shifting (b) After one shift (c) After all shifts

Figure 11. Stair climbing motion for step 3.

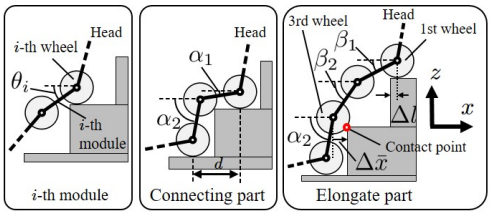

Figure 12. Definition of angles for step 3.

$$\theta_{i+2} = (\beta_1 - \alpha_2)t' + \alpha_2, \tag{10}$$

$$\theta_{i+3} = (\beta_2 - \alpha_1)t' + \alpha_1, \tag{11}$$

$$\theta_i = 2\ \mathrm{atan2}\left(\frac{2L\Delta z - \sqrt{(\Delta x^2 + \Delta z^2)(4L^2 - \Delta x^2 - \Delta z^2)}}{\Delta x^2 + \Delta z^2 + 2L\Delta x}\right), \tag{12}$$

$$\theta_{i+1} = 2\ \mathrm{atan2}\left(\frac{2L\Delta z + \sqrt{(\Delta x^2 + \Delta z^2)(4L^2 - \Delta x^2 - \Delta z^2)}}{\Delta x^2 + \Delta z^2 + 2L\Delta x}\right), \tag{13}$$

where t is time, $t' = 6\tilde{t}^5 - 15\tilde{t}^4 + 10\tilde{t}^3$ is the quintic curve, given as a cam curve, $\tilde{t} = \frac{t}{t_{\mathrm{shift}}}$, $0 \leq t \leq t_{\mathrm{shift}}$, and

$$\Delta x = d + L(\cos\beta_1 + \cos\beta_2) - L(\cos\theta_{i+2} + \cos\theta_{i+3}), \tag{14}$$

$$\Delta z = h + L(\sin\beta_1 + \sin\beta_2) - L(\sin\theta_{i+2} + \sin\theta_{i+3}). \tag{15}$$

If (12) and (13) have a solution without imaginary parts, it is necessary to satisfy the condition $4L^2 - \Delta x^2 - \Delta z^2 \geq 0$. However, (10)–(13) do not guarantee it. Design of $\theta_i, \cdots, \theta_{i+3}$ to satisfy the condition is one of future works.

By carrying out steps 1–3, the robot moves the wheels forward and upward, as Fig. 16 shows. The robot can hence climb the stairs step by step by repeating steps 1–3. In the case of climbing down stairs, we can design the motion in a similar way to the case of climbing up stairs.

In the proposed method, the robot moves while contacting the wheel with the edge of the step, as shown in Fig. 10 (the first wheel in case 1 and the second wheel in cases 2 and 3). As a result, the robot can keep the joint torque needed for climbing down the stairs small. Thus, although the folding arm, which is heavy, is attached to the head of the robot, the robot can execute the motion. However, note that the proposed stair climbing has this merit only in the case where the third wheel in the elongating part contacts with the edge of the step. In addition, note that

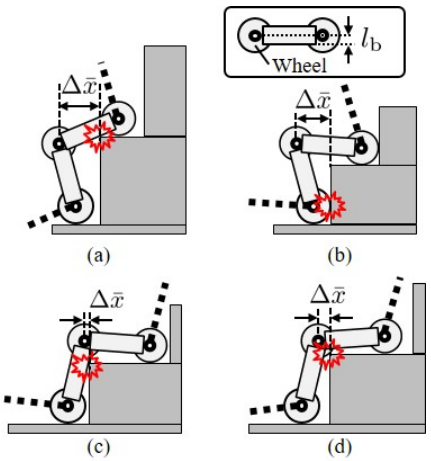

Figure 13. $\Delta\bar{x}$ in the four cases depending on the contact point.

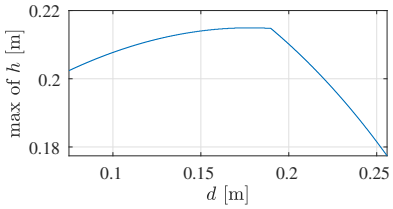

Figure 14. Relationship between d and maximum h when $L = 0.181$, $r = 0.075$, $l_\mathrm{b} = 0.025$, and $\Delta l = 0.01$.

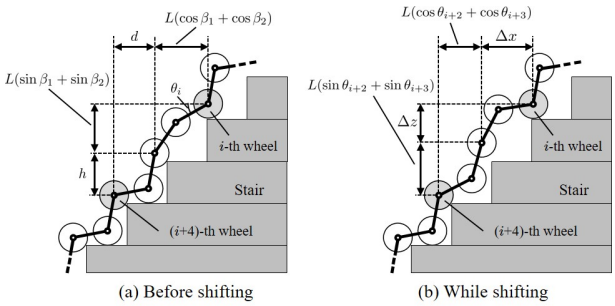

Figure 15. Geometric relationships when shifting the elongating part.

this method can be only used when the parameters of the stairs are known.

We carried out simulations to demonstrate the effectiveness of the proposed method. Figure 17 shows the simulation results using the physical simulator V-REP [34]. We set $L = 0.181$ m, $r = 0.075$m, and $\Delta l = 0.01$ m. In the simulation, we used three parameter sets of stairs, $(d, h) = (0.2, 0.2), (0.24, 0.18), (0.15, 0.21)$ m considering Fig. 14. The robot climbed up and down the stairs using the proposed method. When the robot climbs up the stairs, the tip of the arm leans forward in Fig. 17(a). This is because the joint torque is decreased and the arm is used to appropriately adjust the forward movement in step 1. However, when climbing the stair with $d = 0.15$ m and $h = 0.21$ m, the arm collided the base part because the target angle of the joint was so large. If the proposed method is used for the actual robot, we need to consider such collision and the angle rage of the joint.

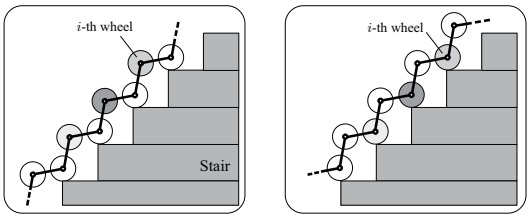

(a) Before (b) After

Figure 16. Robot posture and stairs before and after steps 1–3.

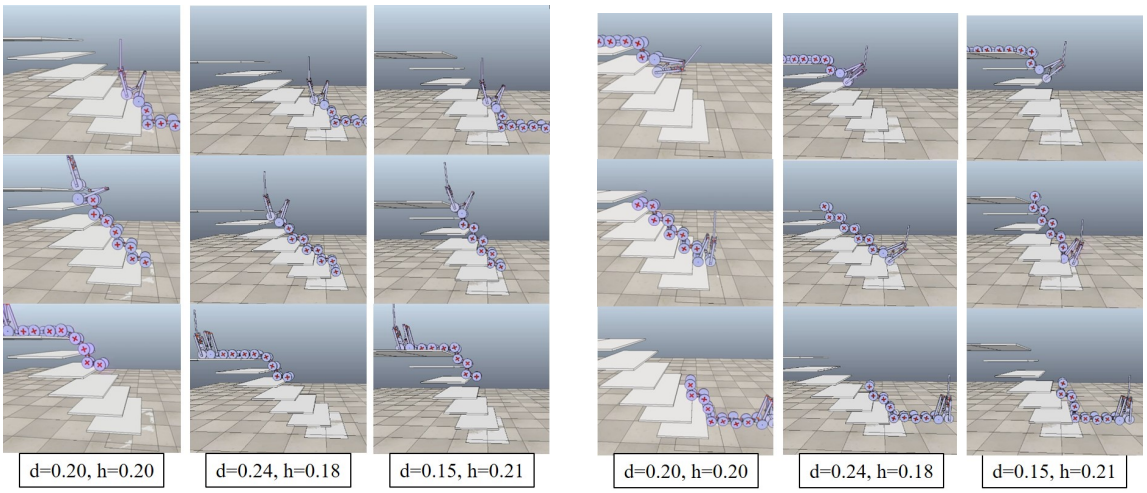

(a) Climbing up (b) Climbing down

Figure 17. Simulation results of stair climbing.

4. User Interface

The proposed robot is not fully autonomous but remotely controlled. Four control modes are implemented on the robot: basic steering control, basic steering with the virtual module, stair climbing, and arm operation. The operator sends the commands, e.g. the motion of the head, switching the control mode, and operating the gripper, to the proposed robot using a gamepad controller.

Figure 18 shows a screenshot of the laptop during operation. The current control mode and current posture of the robot are depicted in the mode and robot area, respectively. The numerical information, e.g. the value of the height of the stair and the length of the virtual module, is depicted in the information area. The error of the actuators e.g. communication, overload, and overheating errors are depicted in the error area. The operator operates the robot while watching the information in addition to the head and tail camera views.

The operator checks the sensor information obtained during the operation of the robot using the graphical user interface (GUI), as shown in Fig. 19. The GUI for sensor information is composed of three windows; (i) image viewer panel, (ii) control panel, and (iii) 3D map viewer panel. Each window is implemented as an independent process, and we used the windows while changing their position and scale according to the contents of the mission. The details of the three panels are as follows.

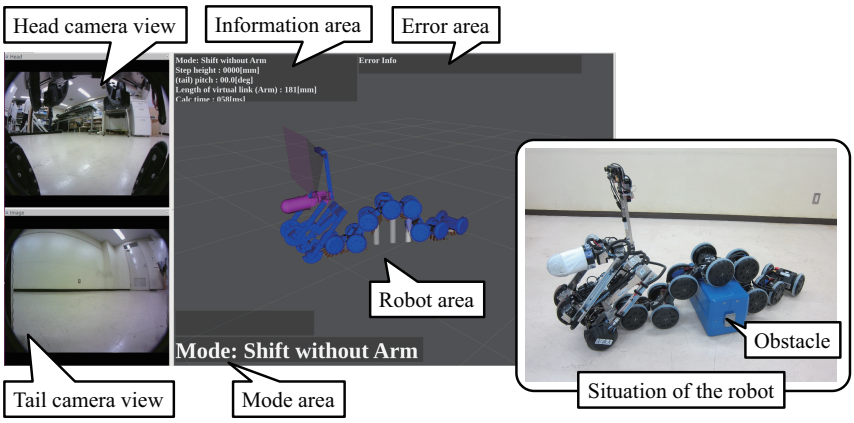

Figure 18. Screenshot of the laptop during operation (left) and the situation of the robot (right).

- *(i) Image viewer panel:* Image viewer panel is composed of two tabs: one displays the image processing results of the visible light camera (Fig. 20(a)) and the other shows the image processing results of the thermal camera (Fig. 20(b)). The tab for the image processing results of the visible light camera can show the results of rust detection and crack detection to help the operator and inspector, e.g. calculate the percentage of rust area, emphasise cracks, and enlarge an image. In the tab for the image processing results of the thermal camera, the images of both the visible light camera and thermal camera are overlaid for abnormal thermal source detection, and the absolute temperature of the point clicked on by a mouse is depicted.
- *(ii) Control panel:* Control of the volume of the speaker, the ability to save log data, and environmental map initialization are provided in the control panel as Fig. 19(a). In addition, information obtained during inspection is displayed as a list.
- *(iii) 3D map viewer panel:* A 3D map that is created by Visual SLAM using the stereo vision camera is displayed in the 3D map viewer panel, as shown in Fig. 19(a). The visual odometry provided by the ZED SDK [35] is used as the front-end of the Visual SLAM, and RTAB-MAP [36] is used as the back-end. The estimated map and estimated path of the robot are represented as a coloured voxel map and arrows, respectively, as Fig. 21 shows. Inspection data is related to the 3D map by representing the points at which sensor data has been saved as markers on the 3D map. In addition, the maximum temperature in the camera view area and CO2 concentration are displayed using the Rviz plugin [37]. If they exceed their preset threshold, the noticeability of an abnormal state is improved by changing the colour of their display, as in the upper right image of Fig. 20. In Fig. 20(b), the temperature of the clicked position is displayed. In contrast, the maximum temperature in the camera view area is displayed in panel (iii). These two displays help the operator to avoid missing the detection of an abnormal temperature.

5. Experiments

5.1 *Mobility*

In these experiments, the operator provided commands by a gamepad while directly looking at the robot rather than looking at the camera images. The experimental results of mobility are shown in Table 3.

The robot crossed a trench of width 600 mm, as Fig. 22(a) shows. In this motion, the dummy wheel touched down on the forward plane by elongating the virtual module, and the robot moved forward by shortening the length of the virtual module. In the case of a trench 650 mm in width,

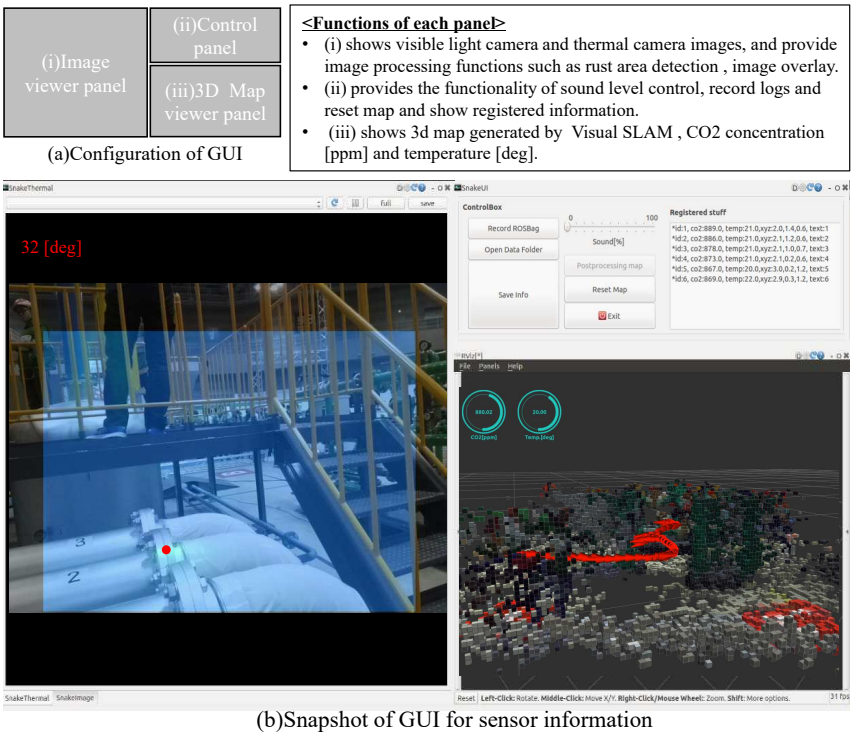

(a)Configuration of GUI

(b)Snapshot of GUI for sensor information

Figure 19. GUI for sensor information management: (a) configuration and (b) screenshot of the GUI.

Table 3. Basic mobility properties of the proposed robot.

Property	Value
Propulsion speed (mm/s)	400
Maximum trench width (mm)	600
Maximum step height without riser (mm)	400
Maximum step height with riser (mm)	600
Minimum width of the L-shaped path (mm)	400

the approach to the forward plane using the virtual module succeeded, but the experiment was discontinued because an overload error on the actuator of the joint occurred when the tail was in a cantilever state. Using the folding arm, the robot can approach the forward plane in a trench that the robot without the arm cannot cross because of the torque limit of the joint. The robot could cross a wider trench using a recovery function from the overload error of the joint.

For the step climbing, we used the basic steering control with the virtual module, and lengthened and shortened the virtual module during the motion. First, the robot accessed the upper plane of the step by lengthening the virtual module, as Fig. 22(b) at $t = 20$ shows. Next, the robot moved forward by shortening the virtual module, as shown in Fig. 22(b) at $t = 40$. As a result, the robot climbed the 400-mm-high step without risers. In the case of a step with a riser, the robot climbed the 600-mm high step, as Fig. 22(c) shows.

In spaces with small widths, we also used the basic steering control with the virtual module. The robot could pass through an L-shaped corridor of width 400 mm, as Fig. 22(d) illustrates.

5.2 *Stair climbing*

Stair climbing experiments were carried out using the method proposed in Section 3.2. The operator provided commands using a gamepad controller while looking directly at the robot. We set $t_{\text{shift}} = 1.5$ s and $\Delta l = 0.02$ m.

Figure 23 shows the motion of the robot climbing up the stairs with $d = 0.2$ m and $h = 0.2$

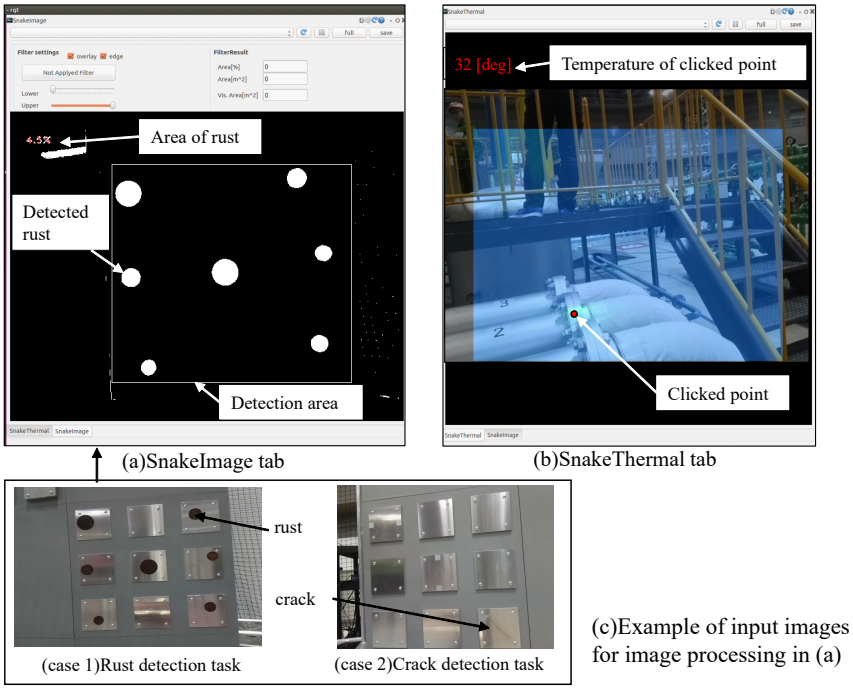

Figure 20. Two tabs from the image viewer panel in Fig. 19: (a) the SnakeImage tab shows the visible light camera image and can show the results of image processing for rust and crack detection and (b) the SnakeThermal tab shows an overlaid image for thermal source detection.

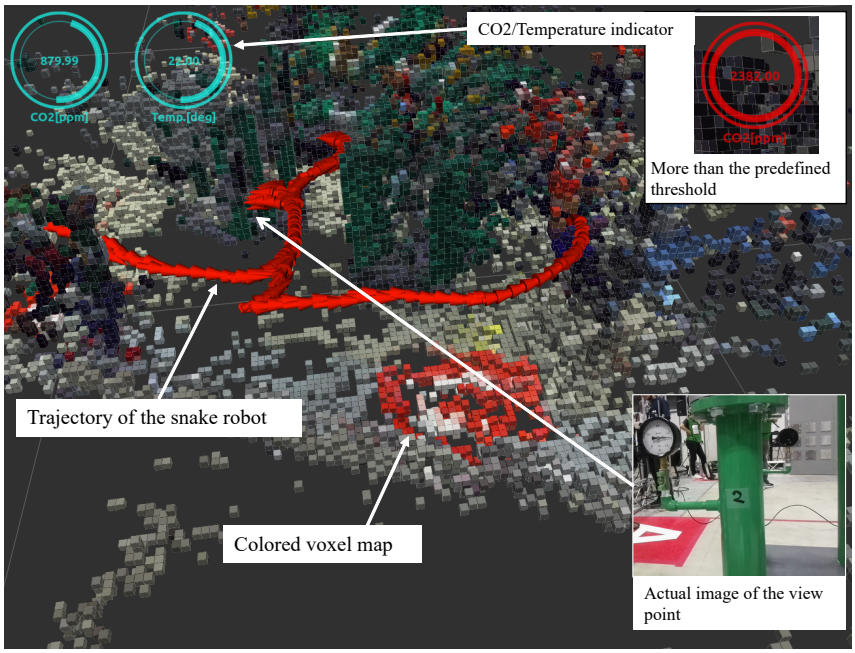

Figure 21. 3D Map Viewer in Fig. 19. This panel shows 3D map generated as a coloured voxel gridmap.

m. The posture of the arm was adjusted to decrease the joint torque similar to the case in the simulations. It was confirmed that the robot could climb the stairs by shifting the elongated part from the head to tail, as shown in Fig. 23(b).

In contrast, the robot could not climb down the stairs, as Fig. 24 shows, because the arm contacted the stairs. This occurred because the fore dummy wheel did not move forward and the posture of the robot did not follow its target. Although the surface of the fore dummy wheel was covered by resin to decrease friction, it seems that the friction force was high because of

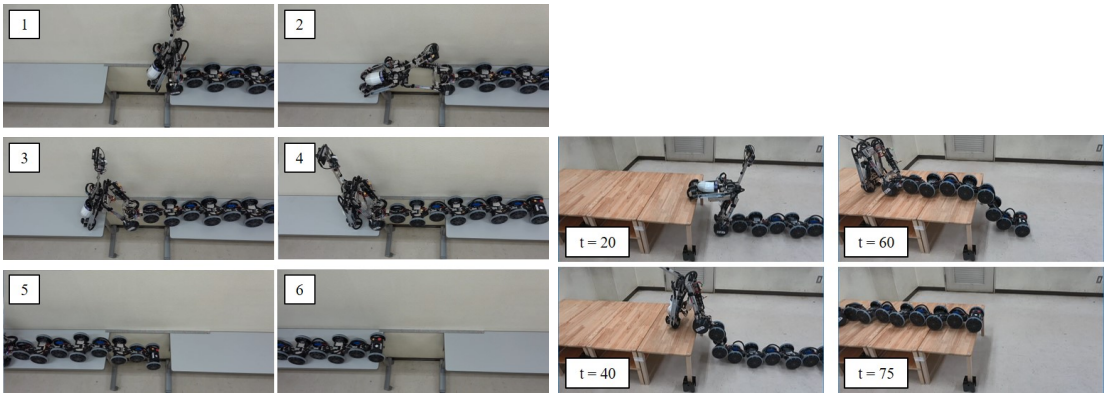

(a) Trench crossing (width = 600 mm)

(b) Step climbing (height = 400 mm without riser)

(c) Step climbing (height 600 = mm with riser)

(d) Passing through an L-shaped corridor (width = 400 mm)

Figure 22. Experimental result of basic mobility

Table 4. Mobility tests in WRS2018.

Tasks	Success/failure
Enter all narrow spaces	Success
Move on a steel grating	Success
Climb up a step (height: 125 mm)	Success
Overcome a slope (angle: 15 degree)	Success
Climb stairs (d =200 mm, h =200 mm)	Failure*
Climb ladder	Unable

*The robot overturned after climbing three steps.

heavy weight of the arm. The improvement of the dummy wheel and target posture of the arm when climbing down stairs is a task for future work.

5.3 *Field test in WRS2018*

The missions of daily inspection and initial fire-fighting as an abnormal situation were carried out in a preliminary round. We changed network between the robot and operator station from a wireless to a wired connection because many teams used WiFi and interference occurred.

Table 4 shows the results of mobility test. The robot climbed the 125-mm high step and entered the 540-mm wide narrow space between pumps, as Fig. 25(a) shows. In this case, basic steering control with the virtual module was used to decrease the joint torque of the robot. Then, the robot inspected the pressure gauge, which was 1.5 m above the floor using the folding arm. As

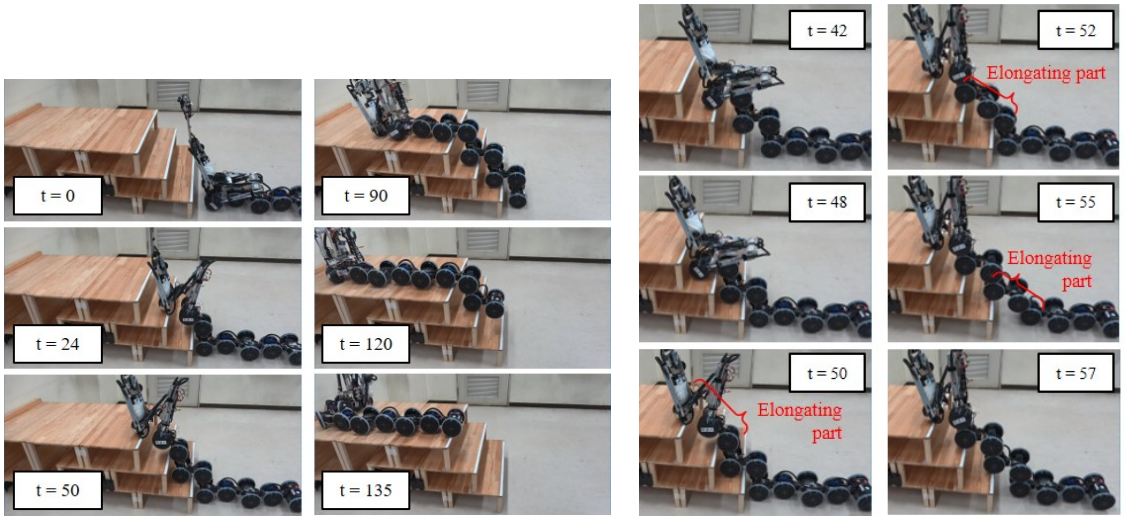

(a) $t = 0, 24, 50, 90, 120, 135$ (b) $t = 42, 48, 50, 52, 55, 57$

Figure 23. Experimental result of climbing up stairs ($d = h = 0.2$ m). Step 1: $t = 42 \leq t \leq 48$, step 2: $48 < t \leq 50$, and step 3: $50 < t \leq 57$.

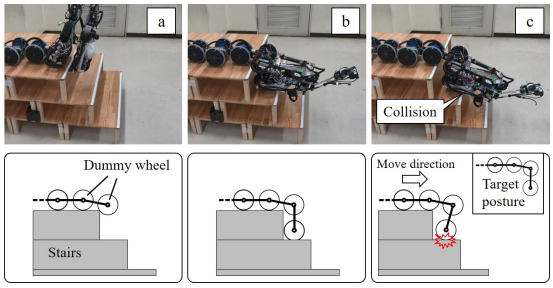

Figure 24. Experimental result of climbing down stairs ($d = h = 0.2$ m).

a test of entering narrow spaces, the robot entered a 425-mm wide space at the side of a tank, as Fig. 25(b) shows, to access the valves of the tank, and the narrow space (about 500 mm in width) under the inspection walkway, as shown in Fig. 25(c), to inspect the pressure gauge of the boiler. In addition, the robot could move on the grating without problems, as Fig. 25(d) shows.

Figure 26 shows the result of stair climbing. The robot fell down after climbing three steps. As a result, the robot could not arrive at the inspection walkway at the top of the stairs. The overturn was caused by the wheel indicated by the red arrow in Fig. 26. The wheel went under the stair and contacted the underside of the tread of the stairs when the robot shifted the elongated part.

Table 5 shows the results of the valve rotating test. The robot could rotate some valves using the folding arm and gripper, as YouTube videos show [38–40]. The details of this test will be presented in [24].

Table 6 shows the results of the inspection and fault detection tests. Figures 27 and 28 show images of the tests. Reading pressure gauges, inspecting the control panel LEDs of pump, reading water level gauges, and the other tasks were successfully completed. In addition, reporting the ratio of rust in designated areas on the lower side of a wall was also accomplished using the image processing for rust detection.

In contrast, there were tasks that the robot could not complete, e.g. identifying areas with concrete flaking and measuring oxygen concentration, because the robot did not have sensors to

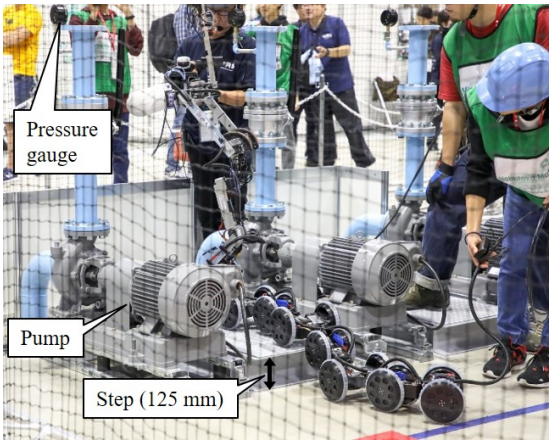

(a) Gauge reading after climbing a step and entering a narrow space.

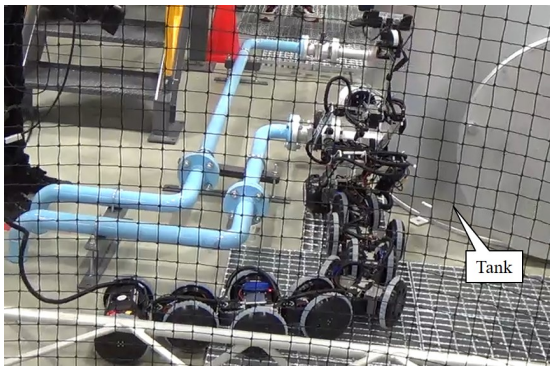

(b) Entering a narrow space between a tank and piping.

(c) Entering a narrow space under an inspection walkway.

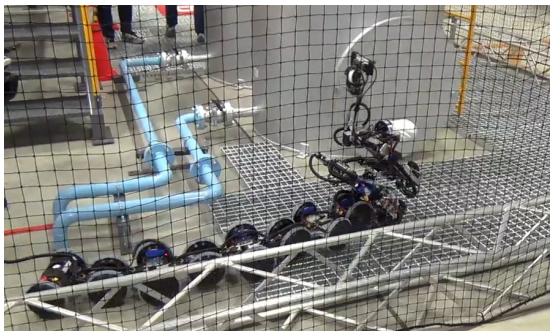

(d) Moving on a grating.

Figure 25. Experimental results in WRS2018.

Table 5. Valve operating tests in WRS2018.

Tasks	Success/failure
50A ball valve	Success [38]
80A ball valve	Unable
15A ball valve*	Success [39]
80A gate valve	Unable
80A rubber seated valve	Partial success**[40]

*The manual starting device of the foam fire extinguishing equipment was at a height of 1.2 m.

**The robot could rotate the valve but the rotation angle was not correct.

measure them. Moreover, when reporting the ratio of rusting, an error was caused by reflected light, and another calculation error occurred because the robot looked up at the inspection area on the upper side of the wall, as Fig. 29 shows.

As described above, these tests confirmed that the robot, which is an articulated mobile type, could navigate, rotate valves, and carry out inspection and fault detection in a mock industrial plant. However, we could not reach the final mission, which was completed by four teams, because the score that the proposed robot system obtained in each mission was half that of the top team. The lessons learned from the field test are as follows.

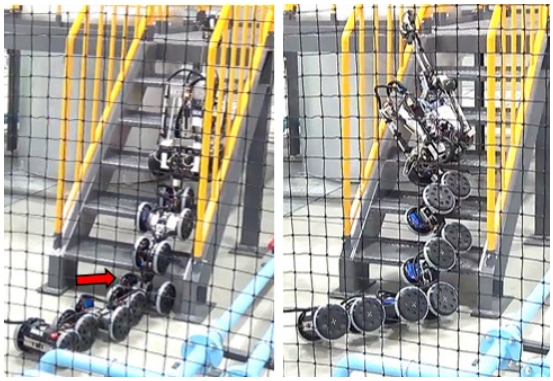

Figure 26. Stair climbing. The left and right pictures show before and after overturning.

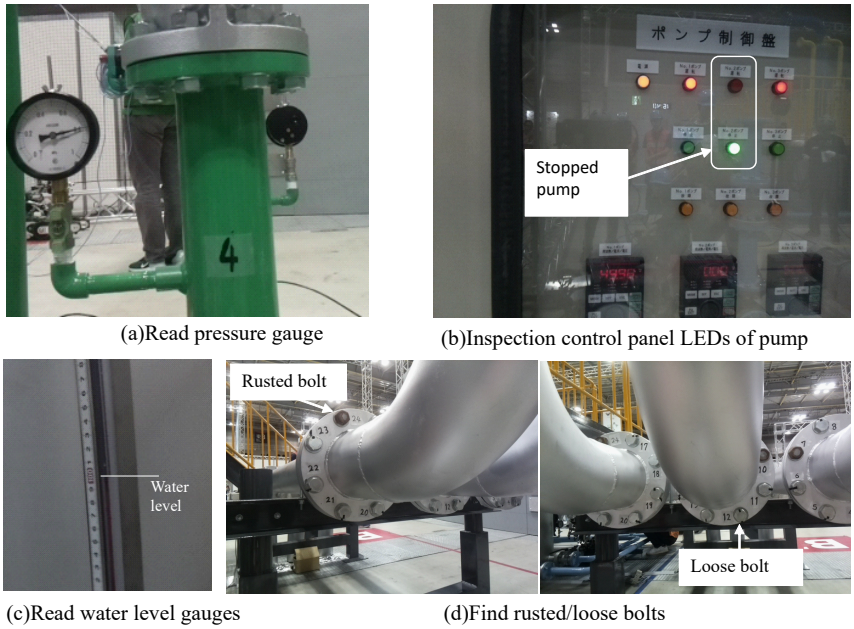

(a)Read pressure gauge (b)Inspection control panel LEDs of pump

(c)Read water level gauges (d)Find rusted/loose bolts

Figure 27. Images of the inspection and fault detection tests in WRS2018. (1/2)

- *Effectiveness of a snake-like robot:* The top three teams used two different types of robot: a crawler robot or a multirotor aerial vehicle, depending on the mission. In contrast, although the inspection speed was not high, we demonstrated that a single snake-like robot could carry out almost the same tasks.
- *Inspection speed:* The robot approached the inspection target using command manually provided the operator. If the position of the inspection target is known, the inspection speed could be increased by improving the autonomous level of the operation of the robot. In addition, the speed of reading gauges could be improved by automation using image processing.
- *Operation when climbing stairs:* In the current system, the operator sends the trigger to shift the connecting part when the robot climbs stairs using the proposed stair climbing method. However, it is difficult for the operator to understand the appropriate timing of the shift and the robot unfortunately fell down when climbing stairs in the field test. A semiautonomous shifting method using sensor data, as in [16], is needed.
- *Ability to adjust camera position:* In the inspection using the visible light camera image, it took a long time to move the camera close enough to the inspection target to be able to inspect because the camera position was manually controlled by the operator using a

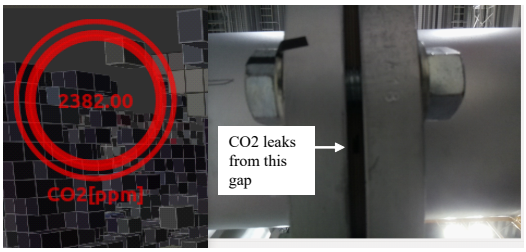

(e)Find gas leakage (carbon dioxide concentration)

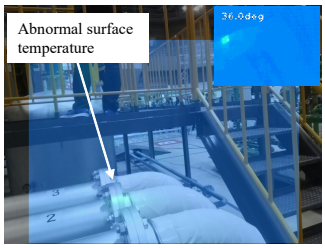

(f)Find abnormalities in the surface temperature of piping

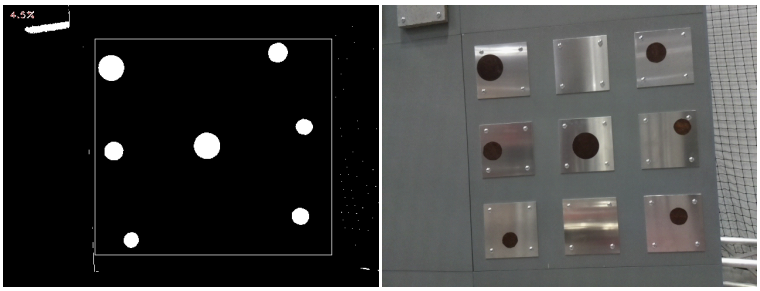

(g)Report the ratio of rusting in designated areas

Figure 28. Images of the inspection and fault detection tests in WRS2018. (2/2)

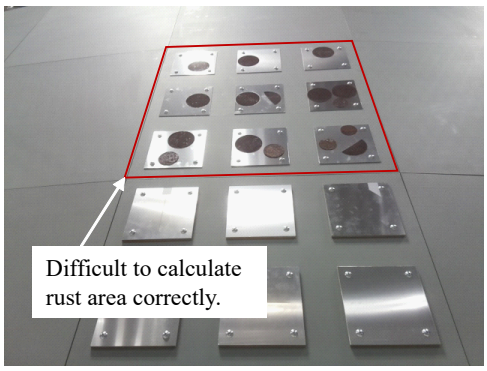

(a)Problem due to the camera view point: In case of inspection area was located on upper side of the wall, it was difficult to find and calculate rust area correctly.

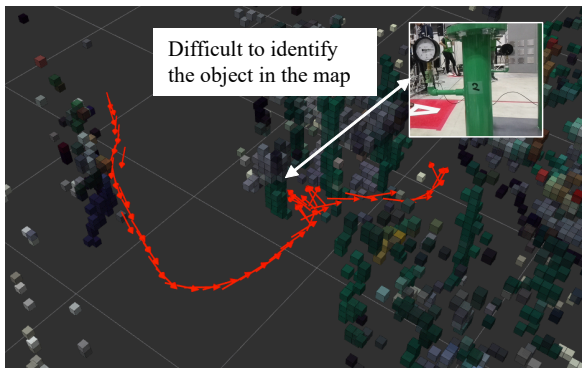

(b)Problem due to low resolution of the map: Due to low resolution, it was difficult to identify the objects on the map.

Figure 29. Problems found in the inspection and fault detection tests in WRS2018.

gamepad controller. A function to autonomously adjust the camera position needs to be implemented or the camera should be replaced with one that has a high resolution or pan-tilt-zoom function.

- *Robustness to lighting conditions and viewpoint:* There were the problems when detecting rust because of the lighting conditions and viewpoint. More robust image processing and autonomous calculation that does not depend on the viewpoint are needed in the system.
- *Calculation of the width and length of cracks:* For the detection of cracks, crack emphasis was implemented, but the system did not have the function to autonomously calculate the width and length of cracks. In addition to introducing the function, it is also necessary to improve its robustness to lighting conditions and viewpoint, as described above.
- *Estimation of the position of a sound source:* We tried to identify an abnormal pump by listening the sound obtained from the microphone, but it failed because the microphone had low directional properties. The ability to estimate the direction of a sound source using a microphone with high directionality or multiple microphones is required.
- *High-definition map:* The location estimation of the robot using Visual SLAM was success-

Table 6. Inspection and fault detection tests in WRS2018.

Tasks	Success/failure
Read pressure gauges	Success*
Inspect yjr control panel LEDs of pumpd	Success*
Read water level gauges	Success*
Find loose bolts	Success*
Find rusted bolts	Success*
Find gas leakage (carbon dioxide concentration)	Success
Find abnormalities in the surface temperature of piping	Success
Measure the oxygen concentration	Unable (no sensor)
Identify an abnormal pump	Failure
Read temperature gauges	Could not try
Report the ratio of rusting in designated areas	Success
Report the width and length of cracks	Unable
Identify areas with concrete flaking (cavities)	Unable

*The operator read the value using the image of the visible light camera.

ful, but we could not generate a map in which the resolution was high enough to detect the inspection target because the map consisted of a point cloud. As a result, it was difficult to identify the inspection target on the generated map. The identification of an inspection target needs to be facilitated by creating a high-definition map or semantic map.

6. Conclusion

We developed the T^2 Snake-4 articulated mobile robot for plant inspection. The robot has sensors for information gathering, a soft gripper for grasping objects, and a folding arm for both reaching high locations and performing tasks, such as valve rotation using the gripper. The stair climbing method using a single backward traveling wave was proposed, and the robot could climb stairs with shallow tread using the proposed method. The mobility of the robot and effectiveness of the proposed stair climbing were demonstrated by experiments. In addition, the proposed robot system was tested in WRS2018. The robot was able to navigate through narrow spaces, read the value of the gauges located 1 m above the floor, and rotate valves.

Future tasks are to put the research results to practical use by improving the system based on the lessons learned and to automate both locomotion and inspection.

Acknowledgements

This work was partially supported by the ImPACT Program of Council for Science, Technology and Innovation (Cabinet Office, Government of Japan) and JSPS KAKENHI Grant Number 18K04011.

References

[1] Shukla A, Karki H. Application of robotics in onshore oil and gas industry–A review Part I. Robotics and Autonomous Systems; 2016; 75: 490-507.
[2] Shukla A, Karki H. Application of robotics in offshore oil and gas industry–A review Part II. Robotics and Autonomous Systems; 2016; 75: 508-524.
[3] ARGOS challenge, `http://www.argos-challenge.com/en`
[4] K. Kydd, S. Macrez, and P. Pourcel, "Autonomous Robot for Gas and Oil Sites," *SPE Offshore Europe Conf. and Exhibition*, Society of Petroleum Engineers, 2015.
[5] World Robot Challenge 2018, `http://worldrobotsummit.org/en/wrc2018/`
[6] Tadokoro S, et al., The World robot summit disaster robotics category - achievements of the 2018 preliminary competition. Advanced Robotics; 2019; DOI: 10.1080/01691864.2019.1627244

[7] Nagatani K, Endo D, Watanabe A, Koyanagi E. Design and Development of Explosion-Proof Tracked Vehicle for Inspection of Offshore Oil Plant. In: Hutter M., Siegwart R. (eds) Field and Service Robotics. Springer Proceedings in Advanced Robotics, vol 5. Springer, Cham; 2018. p.531-544.
[8] Kohlbrecher S, Stryk, O. From RoboCup Rescue to Supervised Autonomous Mobile Robots for Remote Inspection of Industrial Plants. KI-Künstliche Intelligenz; 2016; 30-3: 311-314.
[9] Hutter M, Gehring C, Lauber A, Gunther F, Bellicoso CD, Tsounis V, Fankhauser P, Diethelm R, Bachmann S, Bloesch M, Kolvenbach H, Bjelonic M, Isler L, Meyer K. ANYmal - toward legged robots for harsh environments. Advanced Robotics; 2017; 31-17, 918-931.
[10] Merriaux P, Rossi R, Boutteau R, Vauchey V, Qin L, Chanuc P, Rigaud F, Roger F, Decoux B, Savatier X. The VIKINGS: An Autonomous Inspection Robot for the ARGOS Challenge. IEEE Robotics & Automation Magazine (Early Access). DOI: 10.1109/MRA.2018.2877189
[11] Granosik G. Hypermobile Robots – the Survey. J. of Intelligent and Robotic Systems; 2014; 75-1: 147-169.
[12] Ito K, Maruyama H. Semi-autonomous serially connected multi-crawler robot for search and rescue. Advanced Robotics; 2016; 30-7:489-503.
[13] Borenstein J, Hansen M, Borrell A. The OmniTread OT-4 Serpentine Robot – Design and Performance. J. of Field Robotics; 2007; 24-7:601-621.
[14] Komura H, Yamada H, Hirose S, Endo G, Suzumori K. Development of snake-like robot ACM-R8 with large and mono-tread wheel. Advanced Robotics; 2015; 29-17:1081-1094.
[15] Brown HB, Weghe JMV, Bererton CA, Khosla PK. Millibot Trains for Enhanced Mobility. IEEE/ASME Trans. on Mechatronics; 2002; 7-4: 452-461.
[16] Tanaka M, Nakajima M, Suzuki Y, Tanaka K. Development and Control of Articulated Mobile Robot for Climbing Steep Stairs. IEEE/ASME Trans. on Mechatronics; 2018; 23-2: 531-541.
[17] Tanaka M, Tadakuma K, Nakajima M, Fujita M. Task-Space Control of Articulated Mobile Robots With a Soft Gripper for Operations. IEEE Trans. on Robotics; 2019; 35-1: 135-146.
[18] Fukushima EF, Hirose S, Hayashi T. Basic Manipulation Consideration For The Articulated Body Mobile Robot. In: Proc. IEEE/RSJ Int. Conf. on Intelligent Robots and Systems; 1998; Victoria, Canada. p.386-393.
[19] Fukushima EF, Hirose S. Integration of Locomotion and Manipulation Control for Articulated Body Mobile Robots. J. of Robotics Society of Japan; 2000; 18-8: 1112-1121.(in Japanese with English summary).
[20] Yamada H, Hirose S. Development of Practical 3-Dimensional Active Cord Mechanism ACM-R4. J. of Robotics and Mechatronics; 2006; 18-3: 305-311.
[21] Yamada H, Takaoka S, Hirose S. A snake-like robot for real-world inspection applications (the design and control of a practical active cord mechanism. Advanced Robotics; 2013; 27-1:47-60.
[22] Kouno K, Yamada H, Hirose S. Development of Active-Joint Active-Wheel High Traversability Snake-Like Robot ACM-R4.2. J. of Robotics and Mechatronics; 2013; 25-3:559-566.
[23] Fujita M, Tadakuma K, Komatsu H, Takane E, Nomura A, Ichimura T, Konyo M, Tadokoro S. Jamming Layered Membrane Gripper Mechanism for Grasping Differently Shaped-Objects Without Excessive Pushing Force for Search and Rescue. Advanced Robotics; 2018; 32-11: 590-604.
[24] Matsumoto N, Tanaka M, Nakajima M, Fujita M, Tadakuma K. Development of a folding arm on an articulated mobile robot for plant disaster prevention. Advanced Robotics; submitted.
[25] Yamada H, Hirose S. Study of Active Cord Mechanism –Approximations to Continuous Curves of a Multi-joint Body–. J. of the Robotics Society of Japan; 2008; 26-1:110-120 (in Japanese with English summary).
[26] Kinugasa T, Haji T, Yoshida K, Amano H, Hayashi R, Tokuda K, Iribe M. Development of Flexible Mono-Tread Mobile Track Using Rotational Joints. J. Intelligent & Robotic Systems; 2016; 1-16.
[27] Takita Y, Hasegawa M, Nunobiki M. An investigation of climbing up stairs for an inchworm robot. Advanced Robotics; 2001; 15-2:245-253.
[28] Tesch M, Lipkin K, Brown I, Hatton R, Pech A, Rembisz J, Choset H. Parameterized and Scripted Gaits for Modular Snake Robots. Advanced Robotics; 2009; 23-9:1131-1158.
[29] Takemori T, Tanaka M, Matsuno F. Gait Design of a Snake Robot by Connecting Simple Shapes. In: Proc. IEEE Int. Symp. on Safety, Security, and Rescue Robotics; 2016; Lausanne, Switzerland. p.189-194.
[30] Gray J, Lissmann HW. Studies in Animal Locomotion: VII. locomotory reflexes in the earthworm. J. of Experimental Biology; 1938; 15:506-517.
[31] Marvi H, Bridges J, Hu DL. Snakes mimic earthworms: propulsion using rectilinear travelling waves.

J. of the Royal Society Interface; 2013; 10:1-12.
[32] Menciassi A, Gorini S, Pernorio G, Weiting L, Valvo F, Dario P. Design, Fabrication and Performances of a Biomimetic Robotic Earthworm. In: Proc. IEEE Int. Conf. on Robotics and Biomimetics; 2004; Shenyang, China. p.274-278.
[33] Seok S, Onal CD, Cho KJ, Wood RJ, Rus D, Kim S. Meshworm: A Peristaltic Soft Robot With Antagonistic Nickel Titanium Coil Actuators. IEEE/ASME Trans. on Mechatronics; 2013; 18-5: 1485-1497.
[34] Rohmer E, Singh SPN, Freese M. V-REP: a Versatile and Scalable Robot Simulation Framework. In: Proc. IEEE/RSJ Int. Conf. on Intelligent Robots and Systems; 2013; Tokyo, Japan. p.1321-1326.
[35] ZED SDK, STEREOLABS, https://www.stereolabs.com/developers/
[36] Labbé M, Michaud F. Appearance-Based Loop Closure Detection for Online Large-Scale and Long-Term Operation. IEEE Trans. on Robotics; 2013; 29-3; 734-745.
[37] jsk visualization, https://jsk-visualization.readthedocs.io/en/latest/jsk_rviz_plugins/plugins/pie_chart.html
[38] Plant Disaster Prevention Challenge Day4 (October 20, 2018), https://youtu.be/AzRZnBgJ7ho?t=4702s
[39] Plant Disaster Prevention Challenge Day2 (October 18, 2018), https://youtu.be/ZA8LNPSpeng?t=5412s
[40] Plant Disaster Prevention Challenge Day3 (October 19, 2018), https://youtu.be/gdPEIonKuds?t=19191s